

RE-ACCELERATION OF COSMIC RAY ELECTRONS BY MULTIPLE ICM SHOCKS

HYESUNG KANG

Department of Earth Sciences, Pusan National University, Busan 46241, Korea; hskang@pusan.ac.kr

Received August 4, 2021; accepted August **, 2021

Abstract: Radio relics could be generated by multiple shocks induced in the turbulent intracluster medium during galaxy mergers. Kang (2021) demonstrated that the re-acceleration of cosmic ray (CR) protons via diffusive shock acceleration (DSA) by multiple shocks could enhance the acceleration efficiency and flatten the CR spectrum, compared to a single episode of DSA. Here we examine the CR electron acceleration through multiple re-acceleration by considering energy losses and decompression of the particle distribution and magnetic fields in the postshock region between consecutive shock passages. We find that the accumulated effects of repeated re-acceleration are significant, if preceding shocks are stronger than the last shock and the shock passage interval is $\lesssim 20$ Myr. In such cases, both the CR spectrum and the ensuing radiation spectrum behind the last shock are enhanced and become flatter than the canonical DSA power-law forms. As a result, the shock Mach number estimated from radio observations tends to be higher than the actual Mach number of the last shock. Thus, multiple episodes of DSA may explain the enhanced acceleration efficiency for CR electrons and the discrepancy of shock Mach numbers, $M_X \lesssim M_{\text{rad}}$, inferred for some observed radio relics.

Key words: acceleration of particles — cosmic rays — galaxies: clusters: general — shock waves

1. INTRODUCTION

During the formation of galaxy clusters, shocks with low sonic Mach numbers ($M \lesssim 5$) are expected to form in the hot intracluster medium (ICM) (e.g., Ryu et al. 2003; Vazza et al. 2009, 2011; Hong et al. 2015; Ha et al. 2018a). In particular, merger-driven shocks with $M \sim 1.5 - 3$ have been identified as giant radio relics, such as the Sausage and Toothbrush relics, in the outskirts of merging clusters (van Weeren et al. 2010, 2016). They are interpreted as diffuse synchrotron emitting structures that contain cosmic ray (CR) electrons with Lorentz factor $\gamma_e \sim 10^3 - 10^4$ accelerated via diffusive shock acceleration (DSA) at merger-driven shocks (Kang et al. 2012; Brunetti & Jones 2014; van Weeren et al. 2019).

The Mach numbers of ‘radio relic shocks’, $M_{\text{rad}} = [(3 + 2\alpha_{\text{sh}})/(2\alpha_{\text{sh}} - 1)]^{1/2}$, can be estimated from the radio spectrum, $j_\nu \propto \nu^{-\alpha_{\text{sh}}}$, with the spectral index, $\alpha_{\text{sh}} = (q - 3)/2$, immediately behind the shock (e.g., van Weeren et al. 2010). This is based on the DSA power-law spectrum of CR electrons, $f_{\text{sh}} \propto p^{-q}$, where $q = 4M^2/(M^2 - 1)$ (Drury 1983). Alternatively, one can use the steepening of the volume-integrated synchrotron spectrum, $J_\nu \propto \nu^{-\alpha_{\text{int}}}$, toward the slope, $\alpha_{\text{int}} = \alpha_{\text{sh}} + 0.5$, at high frequencies owing to synchrotron and inverse-Compton (iC) losses in the postshock region. This results in $M_{\text{rad}} = [(\alpha_{\text{int}} + 1)/(\alpha_{\text{int}} - 1)]^{1/2}$ (e.g., Kang 2011).

On the other hand, the Mach numbers inferred from X-ray observations, M_X , are sometimes smaller than M_{rad} , that is, $M_X \lesssim M_{\text{rad}}$, which is considered

as one of the unsolved problems in understanding the origin of radio relics (e.g., Akamatsu & Kawahara 2013; van Weeren et al. 2019). Possible solutions to explain this puzzle suggested so far include re-acceleration of preexisting fossil CR electrons with a flat spectrum (e.g., Kang 2016; Kang et al. 2017) and *in situ* acceleration by an ensemble of shocks with different Mach numbers formed in the turbulent ICM (e.g., Hong et al. 2015; Roh et al. 2019; Domínguez-Fernández et al. 2021; Inchingolo et al. 2021). In fact, recent high-resolution radio observations of some radio relics revealed rich, complex structures, often with filamentary features, indicating the possible presence of multiple shocks (e.g., Di Gennaro et al. 2018; Rajpurohit et al. 2020).

CR electrons are expected to be pre-accelerated and injected to the DSA process only at supercritical ($M \gtrsim 2.3$), quasi-perpendicular (Q_\perp) shocks with the magnetic field obliquity angle, $\theta_{\text{Bn}} \gtrsim 45^\circ$. Electrons gain energy through the gradient-drift along the motional electric fields, being confined near the shock front through scattering off self-excited waves. The electron firehose instability (EFI) in the upstream region (Guo et al. 2014; Kang et al. 2019) and the Alfvén ion cyclotron (AIC) instability in the shock transition zone (Trotta & Burgess 2019; Ha et al. 2021; Kobzar et al. 2021) play important roles in generating multi-scale waves. On the other hand, it had been suggested that pre-existing magnetic fluctuations in the preshock region could facilitate particle injection to DSA (e.g. Guo & Giacalone 2015). Although electron pre-acceleration in the turbulent ICM has yet to be understood, here we presume that electrons could be accelerated even at subcritical

CORRESPONDING AUTHOR: H. Kang

shocks (Kang 2020).

Several previous studies suggested that a CR spectrum flatter than p^{-4} could be produced by multiple passages of shocks (e.g., White 1985; Achterberg 1990; Schneider 1993; Melrose & Pope 1993; Gieseler & Jones 2000). Recently, we have estimated the spectrum of CR protons accelerated by a sequence of shocks with different Mach numbers by adopting the following assumptions (Kang 2021, Paper I, hereafter). (1) DSA operates in the two different modes, *in situ injection/acceleration* mode and *re-acceleration* mode. (2) Even subcritical shocks with $M \lesssim 2.3$ could accelerate CRs via DSA, providing that the ICM contains pre-existing magnetic turbulence on the relevant kinetic scales. (3) In the postshock region, CRs are transported and decompressed adiabatically without energy losses and escape from the system, so the particle momentum, p , decreases to $p' = Rp$, where R is the decompression factor. Paper I suggested that the re-acceleration by multiple shocks could possibly explain the discrepancy, $M_X \lesssim M_{\text{rad}}$ for some radio relics, if they are produced by multiple passages of shocks with the time intervals shorter than the electron cooling timescales. In this study, we explore such a scenario, considering the synchrotron/iC losses in the postshock region.

In the next section we describe the semi-analytic approach to follow DSA by multiple shocks and the models to handle the decompression and cooling in the postshock region. In Section 3, we apply our approach to a few examples, where the re-acceleration by several weak shocks of $M \leq 3$ and the ensuing radio emission spectra are estimated. A brief summary will be given in Section 4.

2. DSA SPECTRUM BY MULTIPLE SHOCKS

We consider a sequence of consecutive shocks that propagate into the upstream gas of the temperature, T_1 , and the hydrogen number density, n_1 . Hereafter, the subscripts, 1 and 2, denote the preshock and postshock states, respectively. The ICM plasma is assumed to consist of fully ionized hydrogen atoms and free electrons, so the preshock thermal pressure is $P_1 = 2n_1 k_B T_1$ and the normalization of the electron distribution function, $f(p)$, scales with n_1 (where k_B the Boltzmann constant).

Figure 1 illustrates the basic concept of DSA by multiple shocks adopted in Paper I, which is implemented with the postshock electron cooling in this study. Below we provide only brief descriptions in order to make this paper self-contained.

2.1. Injected Spectrum at Each Shock

Since the thickness of the shock transition zone is of the order of the gyroradius of the postshock thermal protons, both protons and electrons need to be pre-accelerated to suprathermal momenta greater than the so-called injection momentum,

$$p_{\text{inj}} = Q_p \cdot p_{\text{thp}} \quad (1)$$

in order to diffuse across the shock transition layer and fully participate in the DSA process (e.g., Caprioli et al. 2015; Ryu et al. 2019; Kang 2020). Here $p_{\text{thp}} = \sqrt{2m_p k_B T_2}$ and $Q_p \approx 3.5 - 3.8$ is the injection parameter (e.g., Kang & Ryu 2010; Caprioli et al. 2015; Ha et al. 2018b). Throughout the paper, common symbols in physics are used: e.g., m_p for the proton mass, m_e for the electron mass, and c for the speed of light. Adopting the traditional thermal leakage injection model (Kang et al. 2002), the distribution function of the injected/accelerated CR protons can be approximated for $p \geq p_{\text{inj}}$ as

$$f_{\text{inj,p}}(p) \approx \left[\frac{n_2}{\pi^{1.5}} p_{\text{thp}}^{-3} \exp(-Q_p^2) \right] \left(\frac{p}{p_{\text{inj}}} \right)^{-q} \exp\left(-\frac{p^2}{p_{\text{max}}^2}\right), \quad (2)$$

where p_{max} is the maximum DSA-accelerated momentum. Then the CRp injection fraction is determined by Q_p and q as

$$\xi \equiv \frac{n_{\text{CRp}}}{n_2} \approx \frac{4}{\sqrt{\pi}(q-3)} Q_p^3 \exp(-Q_p^2). \quad (3)$$

Since ξ is expected to increase with the shock Mach number (Ha et al. 2018b), Q_p should be smaller for higher M . However, the quantitative behavior of $Q_p(M)$ based on plasma kinetic simulations has not been fully explored yet. Thus we adopt a constant value, $Q_p = 3.8$ for simplicity, since the main focus of this study is to examine the qualitatively effects of multiple shocks.

The electron injection at Q_{\perp} -shocks are known to involve the following key processes (e.g., Guo et al. 2014; Kang et al. 2019; Trotta & Burgess 2019; Ha et al. 2021; Kobzar et al. 2021): (1) the reflection of some of incoming electrons at the shock ramp due to magnetic deflection, leading to the excitation of upstream waves through the EFI, (2) the generation of ion-scale waves via the AIC due to the dynamics of the reflected protons in the shock transition zone, (3) the energy gain due to the gradient-drift along the motional electric field in the shock transition zone. Thus the electron pre-acceleration occurs mainly through the so-called shock drift acceleration (SDA), rather than DSA.

Several numerical studies of electron pre-acceleration have indicated that a suprathermal tail develops with the power-law form, p^{-q} , for $p \gtrsim p_{\text{ref}}$, which extends above the DSA injection momentum $p > p_{\text{inj}}$ (Guo et al. 2014; Park et al. 2015; Trotta & Burgess 2019; Kobzar et al. 2021). Here, p_{ref} represents the lowest momentum of the reflected electrons (see Figure 1 of Kang 2020). This is again parameterized as

$$p_{\text{ref}} = Q_e \cdot p_{\text{the}}, \quad (4)$$

where $p_{\text{the}} = \sqrt{2m_e k_B T_2}$ is the postshock electron thermal momentum, and so $p_{\text{inj}}/p_{\text{ref}} = \sqrt{m_p/m_e} \approx 43$ (see Figure 2). Then the spectrum of injected electrons is

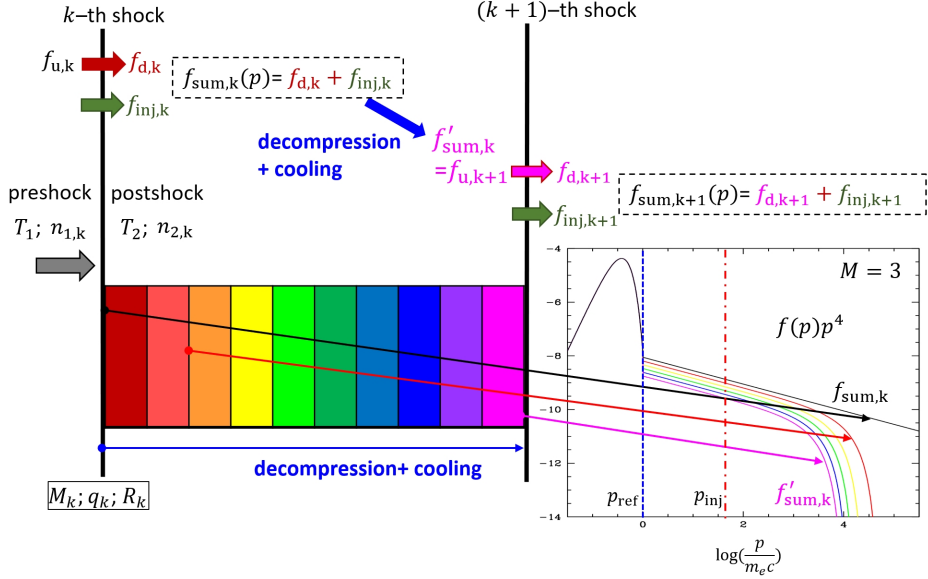


Figure 1. Basic concept of DSA by multiple shocks adopted in this study. The postshock spectrum, $f_{sh}(p) = f_{sum,k}(p)$, consists of the downstream spectrum, $f_{d,k}(p)$, of the re-accelerated CRs, and the injection spectrum, $f_{inj,k}(p)$, of the injected CRs at the k -th shock. Then, decompression and cooling of the postshock CR electrons result in the far-downstream spectrum, $f'_{sum,k}(p)$, which becomes the upstream CR spectrum, $f_{u,k+1}(p)$, at the $(k+1)$ -th shock. The particle spectra, $f(p)p^4$, shown in the right panel illustrate the decompressed and cooled spectra at different locations behind the shock. The blue vertical line denotes $p_{ref} = Q_e \cdot p_{the}$ with $Q_e = 3.8$, above which suprathermal electrons are reflected at the shock ramp, while the red vertical line marks the injection momentum, $p_{inj} = Q_p \cdot p_{thp}$ with $Q_p = 3.8$, for DSA.

assumed to follow the DSA power-law for $p \geq p_{ref}$:

$$f_{inj,e}(p) \approx \left[\frac{n_2}{\pi^{1.5}} p_{the}^{-3} \exp(-Q_e^2) \right] \cdot \left(\frac{p}{p_{ref}} \right)^{-q} \exp\left(-\frac{p^2}{p_{eq}^2}\right). \quad (5)$$

Note that the electrons with $p_{ref} \lesssim p \lesssim p_{inj}$ are referred as ‘suprathermal’ electrons, whereas those with $p \gtrsim p_{inj}$ are defined as CR electrons. Again the quantitative estimation for $Q_e(M)$ has yet to come, so we adopt the same injection parameter $Q_e = 3.8$ as Q_p , which results in the CRE to CRp number ratio, $K_{e/p} = (m_e/m_p)^{(q-3)/2}$, for $p \geq p_{inj}$. Hereafter, we focus on CR electrons and omit the character ‘e’ from the subscript, i.e., $f_{inj,e}(p) = f_{inj}(p)$. So the spectrum of CR electrons injected/accelerated at the k -th shock will be represented by $f_{inj,k}(p)$.

From the equilibrium condition that the DSA momentum gains per cycle are equal to the synchrotron/iC losses per cycle, a maximum momentum can be estimated as follows (Kang 2011):

$$p_{eq} = \frac{m_e^2 c^2 u_s}{\sqrt{4e^3 q/27}} \left(\frac{B_1}{B_{e,1}^2 + B_{e,2}^2} \right)^{1/2}. \quad (6)$$

Here $B_e^2 = B^2 + B_{rad}^2$ is the ‘‘effective’’ magnetic field strength, and $B_{rad} = 3.24 \mu\text{G}(1+z)^2$ takes into account the iC cooling due to the cosmic background radiation at redshift z , and B is given in units of μG . We set $z = 0.2$ as a reference epoch, and so $B_{rad} = 4.7 \mu\text{G}$.

For typical ICM shock parameters,

$$\frac{p_{eq}}{m_e c} \approx \frac{2 \times 10^9}{q^{1/2}} \left(\frac{u_s}{3 \times 10^3 \text{ km s}^{-1}} \right) \left(\frac{B_1}{B_{e,1}^2 + B_{e,2}^2} \right)^{1/2}. \quad (7)$$

2.2. Re-accelerated Spectrum at Subsequent Shock

The upstream spectrum of the k -th shock, $f_{u,k}(p)$, contains the electrons injected and re-accelerated by all previous shocks, which are decompressed and cooled in the postshock region behind the $(k-1)$ -th shock. Then, the downstream spectrum, $f_{d,k}(p)$, re-accelerated at the k -th shock, can be calculated by the following re-acceleration integration (Drury 1983):

$$f_{d,k}(p, p_{ref,k}) = q_k \cdot p^{-q_k} \int_{p_{ref,k}}^p t^{q_k-1} f_{u,k}(t) dt. \quad (8)$$

Again we assume for simplicity that suprathermal electrons with $p_{ref,k} \lesssim p \lesssim p_{inj,k}$ can be re-accelerated via DSA in the same way as for $p \gtrsim p_{inj,k}$, although the re-acceleration of these suprathermal electrons has not been fully explored through plasma simulations. An alternative choice for the lower bound of the integral is $p_{inj,k}$, since only particles above the injection momentum could diffuse back and forth across the shock transition and fully participates in DSA. The result of the re-acceleration integral, $f_{d,k}(p)$, depends somewhat weakly on the the lower bound of the integral, as illustrated in Figure 2. The exponential cutoff, $\exp(-p^2/p_{eq}^2)$, should be applied to Equation (8) as well.

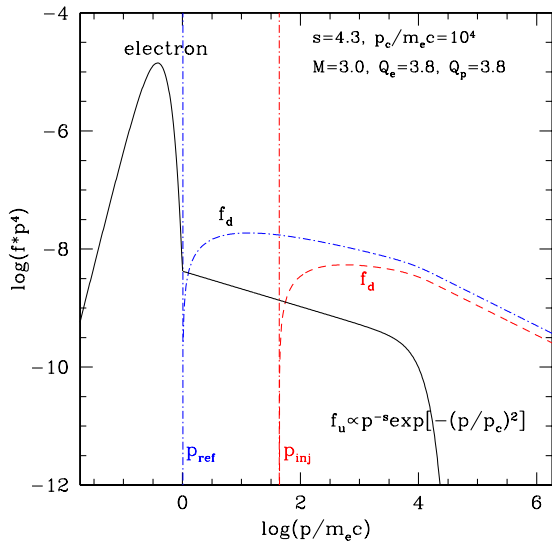


Figure 2. Re-accelerated spectrum, $p^4 f_d$, in a $M = 3$ shock, based on the test-particle DSA model. The black solid line shows a power-law spectrum of pre-existing fossil electrons, $p^4 f_u$, with the power-law slope, $s = 4.3$, and the cutoff momentum, $p_c/m_e c = 10^4$. The blue dot-dashed line shows the spectrum of re-accelerated electrons with the lower bound at p_{ref} , while the red dashed line shows the spectrum with the lower bound at p_{inj} . This illustrates how $f_d(p)$ depends on the lower bound of the re-acceleration integral in Equation (8).

2.3. Decompression and Cooling in the Postshock Region

2.3.1. Decompression Model

As in Paper I, the immediate postshock spectrum, $f_{\text{sum},k}(p) = f_{\text{inj},k}(p) + f_{d,k}(p)$, is decompressed by the decompression factor, $R_k = (D/r_k)^{1/3}$, where $r_k = 4M_k^2/(M_k^2 + 3)$ is the compression ratio at the k -th shock, and at the same time cooled by the synchrotron/iC losses, resulting in the far-downstream spectrum, $f'_{\text{sum},k}(p)$. The right panel of Figure 1 illustrates the combined effects of decompression and cooling with the color-coded lines, depending on the postshock distance behind the shock. Here, the background density factor, $D = 1$, will be adopted in order to minimize the number of free parameters in the problem.

The decompression of the CR electrons and magnetic field strength behind each shock is followed with the advection time, t , with $p' = R'_k(t)p$ and $B'_2(t) = R'_{B,k}(t)B_2$. The evolution of the decompression factors is modeled linearly with t : $R'_k(t) = 1 - (1 - R_k)(t/t_{p,k})$ and $R'_{B,k}(t) = 1 - (1 - R_{B,k})(t/t_{p,k})$, where $R_k = r_k^{-1/3}$, $R_{B,k} = r_k^{-1}$, and $t_{p,k}$ is the passage time between the k -th and $(k + 1)$ -th shocks.

2.3.2. Postshock Aging Model

In Paper I, we considered a scenario, in which CR protons are accelerated by multiple passages of ICM shocks induced during the course of the large-scale structure formation with the mean passage time between two consecutive shocks of $t_p \sim 3 \times 10^8$ yrs. With a typical

speed, $V_s \sim 3 \times 10^3$ km s $^{-1}$, the mean distance between shocks corresponds to $L \approx V_s t_p \sim 1$ Mpc. In the case of CR electrons, this mean passage time is longer than the radiative cooling time of radio-emitting electrons,

$$t_{\text{rad}}(\gamma_e) \approx 9.8 \times 10^7 \text{ yrs} \left(\frac{5 \mu\text{G}}{B_e} \right)^2 \left(\frac{\gamma_e}{10^4} \right)^{-1}. \quad (9)$$

Thus, the effects of multiple shock passages, i.e., flattening and amplification of the energy spectrum, will mostly disappear, because the upstream CR spectrum contains mostly cooled low-energy electrons with $\gamma_e \lesssim 10^3$ (see the blue dotted lines in panels (b.1)-(d.1) of Figure 3).

Instead, here we consider a scenario more relevant to multiple shocks associated with a single merger event that formed in the turbulent ICM (e.g. Roh et al. 2019; Domínguez-Fernández et al. 2021). Recently, Inchinolo et al. (2021) have shown that radio relics could be produced by CR electrons that are swept by multiple shock passages in a sample merging cluster identified in the cosmological MHD simulations. For canonical examples, we assume that the shock passages are separated by $t_{p1} = t_{p2} \approx 5 - 20$ Myr between the first and second shocks and between the second and third shocks. However, the third shock should continue at least for $t_{p3} \sim 10^8$ yrs in order to accumulate the postshock distance of ~ 100 kpc, enough to cover typical widths of giant radio relics.

For synchrotron cooling, we adopt the so-called JP model, in which the pitch-angle distribution of CR electrons is assumed to be continuously isotropized due to scattering off magnetic fluctuations on all relevant scales (Jaffe & Perola 1973). Then, cooling of the postshock electron population is treated by solving the following advection equation in momentum space:

$$\frac{dg}{dt} - C(t)p \cdot \frac{\partial g}{\partial y} = 0, \quad (10)$$

where $g(x, p) = f(x, p)p^4$, $y = \ln(p/m_e c)$, $C(t) = (4e^4/9m_e^4 c^6)B_e(t)^2$ in cgs units, and $B_e(t)^2 = B'_2(t)^2 + B_{\text{rad}}(z)^2$ (Kang et al. 2012). Moreover, we assume that the shock is a planar surface where CR electrons are continuously injected/accelerated and re-accelerated, and that the postshock region is composed of sequential slabs with the decompressed magnetic field, $B'_2(x)$, and the CR electron distribution, $f(x, p)$, with different ages. Figure 1 illustrates how the postshock spectrum, $f_{\text{sh}}(p) = f_{\text{sum},k}(p)$, evolves to $f'_{\text{sum},k}(x, p)$, in the downstream region due to the postshock decompression and cooling.

In the case of the *in situ* injection, the volume-integrated energy spectrum can be found analytically from a simple integration, $F(p) = \int_0^{t_{\text{age}}} f(p, t)u_2 dt$, where t_{age} is the shock age. Note that the shock is assumed to provide the continuous injection (CI) of accelerated CR electrons, because the acceleration time scale of radio-emitting electrons are much shorter than dynamical time scales of order of 10 – 100 Myr. The

Table 1
Model Parameters

Model	M_1, M_2, M_3	$t_{p1,2}$ (Myr)	B_1 (μG)
A	3, 2.7, 2.3	5, 20, 100	0.01, 0.1, 1, 2
B	2.3, 2.7, 3	5, 20, 100	1
C	2.5, 2, 1.7	5, 20, 100	1
D	1.7, 2, 2.5	5, 20, 100	1
E	3, 3, 3	5, 20, 100	1

The third shock lasts for $t_{p3} = 100$ Myr in all models.

integrated spectrum is steeper than the power-law in Equation (5) by one power of the momentum above the ‘break momentum’, i.e., $F(p) \propto p^{-(q+1)}$ for $p \gtrsim p_{\text{br}}$, which can be estimated from the condition $t_{\text{age}} = t_{\text{rad}}$. The corresponding ‘break Lorentz factor’ can be approximated as

$$\gamma_{e,\text{br}}(t) \approx 10^4 \left(\frac{t_{\text{age}}}{10^8 \text{ yrs}} \right)^{-1} \left(\frac{B_e}{5 \mu\text{G}} \right)^{-2}. \quad (11)$$

2.4. Synchrotron Emission from Postshock Electrons

The synchrotron emission from mono-energetic electrons with γ_e peaks around the characteristic frequency,

$$\nu_{\text{peak}} \approx 0.3 \frac{3eB}{4\pi m_e c} \gamma_e^2 \approx 0.38 \text{GHz} \left(\frac{\gamma_e}{10^4} \right)^2 \left(\frac{B}{3 \mu\text{G}} \right). \quad (12)$$

The synchrotron radiation spectrum emitted by the power-law population in Equation (5) has the power-law form, $j_\nu \propto \nu^{-\alpha_{\text{sh}}}$, where $\alpha_{\text{sh}} = (q - 3)/2 = 0.5(M^2 + 3)/(M^2 - 1)$ (Kang 2015).

The volume-integrated radio spectrum, J_ν , calculated with $F(p)$ is expected to steepen to $\alpha_{\text{int}} = \alpha_{\text{sh}} + 0.5$ for $\nu \gtrsim \nu_{\text{br}}$, that corresponds roughly to the characteristic frequency of the electrons with $\gamma_{e,\text{br}}$. Inserting Equation (11) into Equation (12) results in

$$\nu_{\text{br}} \approx 0.38 \text{GHz} \left(\frac{t_{\text{age}}}{10^8 \text{ yrs}} \right)^{-2} \left(\frac{B_e}{5 \mu\text{G}} \right)^{-4} \left(\frac{B}{3 \mu\text{G}} \right). \quad (13)$$

Note that the transition of the spectral index of J_ν from α_{sh} to $\alpha_{\text{sh}} + 0.5$ occurs rather gradually over the broad frequency range, $\nu \sim 0.01 - 1$ GHz, because more abundant lower energy electrons also contribute to the emission at ν_{br} (see Figure 1 of Carilli et al. (1991)).

3. RESULTS

3.1. Model Parameters

As in Paper I, we consider the ICM plasma that consists of fully ionized hydrogen atoms and free electrons with $T_1 = 5.8 \times 10^7$ K (5 keV) and $n_1 = 10^{-4} \text{ cm}^{-3}$. The normalization of $f(p)$ presented in the figures below scales with n_1 .

We consider the models with three shocks specified with Mach numbers, M_1, M_2 , and M_3 , to explore how the strength of preceding shocks affect the CR spectrum at the third shock. Effects of multiple shocks are

expected to depend on the time between two consecutive shock passages and the magnetic field strength. Time intervals, $t_{p1,2} = t_{p1} = t_{p2} \approx 5 - 100$ Myr are considered. The third shock is assumed to last for $t_{p3} \approx 100$ Myr to produce the postshock region of ~ 100 kpc, as observed in typical giant radio relics (e.g. van Weeren et al. 2010, 2016). The fiducial value of the preshock magnetic field is set as $B_1 = 1 \mu\text{G}$. Table 1 summarizes the model parameters considered in this study.

For MHD shocks, the postshock magnetic field strength depends on M and θ_{Bn} . In Q_\perp shocks, $B_2 \approx rB_1$, so, for instance, $B_2 \approx 3 \mu\text{G}$ for $M=3$ ($r = 3$). Since the effective field strength in the postshock region, $B_{e,2} = (B_2^2 + B_{\text{rad}}^2)^{1/2}$ with $B_{\text{rad}} = 4.7 \mu\text{G}$ ($z = 0.2$), the electron cooling remains significant even for weak magnetic fields with $B_1 \ll 1 \mu\text{G}$. On the other hand, the break frequency in Equation (13) scales with B_2 , as long as $B_{e,2} \sim 5 \mu\text{G}$, and so it decreases to $\nu_{\text{br}} \sim 1$ MHz for $B_1 \sim 0.01 \mu\text{G}$.

3.2. Electron Spectrum Accelerated by Multiple Shocks

Figure 3 shows the CR spectrum in four models: model E ($M = 3$) without cooling, with $t_{p1,2} = 5$ Myr, and 20 Myr, and model A with $t_{p1,2} = 5$ Myr. Panels (a.1)-(d.1) show the downstream spectrum, $f_{\text{sh}} = f_{\text{sum},k}$ (solid lines), and the far-downstream spectrum, $f'_{\text{sum},k}$ (dotted lines). Panels (a.2)-(d.2) show the power-law slopes, $q_{\text{sh}} = -\partial(\ln f_{\text{sh}})/\partial(\ln p)$ (solid lines) and $q'_{\text{sum}} = -\partial(\ln f'_{\text{sum}})/\partial(\ln p)$ (dotted lines). Panels (a.1)-(a.2) demonstrate the effects of DSA by multiple shocks, i.e., amplification and flattening of the CR spectrum, when energy losses are ignored.

Panels (a.1)-(c.1) show that, for $\gamma_e \approx 10^4$, the amplitude of $f_{\text{sh}}(p)$ increases by a factor of about 5 – 10 at each passage of a $M \sim 3$ shock, while panel (d.1) shows that the amplification factor is about 2 for a $M = 2.3$ shock. However, panels (b.2)-(d.2) indicate that flattening of $f_{\text{sh}}(p)$ almost disappear for higher energy electrons with $\gamma_e > 10^4$, when postshock cooling is included. The shock slope at the third shock, $q_{\text{sh},3}$ (blue solid), is smaller (flatter) than the DSA slope, $q_3 = 3r_3/(r_3 - 1)$, for low-energy electrons with $\gamma_e \lesssim 10^4$, retaining the flattening effect of multiple shock passages. In the case of the far-downstream spectrum, $f'_{\text{sum},3}(p)$, behind the third shock (blue dotted lines), the flattening effects disappear for $\gamma_e \gtrsim 10^3$. Thus, Figure 3 demonstrates that spectral flattening due to multiple shocks could remain significant for $t_{p1,2} \lesssim 20$ Myr, while the amplification factor of CR spectrum at $\gamma_e \approx 10^4$ can range 2 – 10, depending on the shock Mach number ($M \lesssim 3$).

In Figure 4, model A with $t_{p1,2} = 20$ Myr (left column), and $t_{p1,2} = 5$ Myr (middle column), and model B with $t_{p1,2} = 5$ Myr (right column) are presented. Panels (a.1)-(c.1) show the volume-integrated energy spectrum, $F(p)p^4$, at each shock and the postshock spectrum, $f_{\text{sh}}(p)p^4$, at the third shock. Panels (a.2)-(c.2) show $q_{\text{int}} = -\partial(\ln F)/\partial(\ln p)$ and $q_{\text{sh},3} = -\partial(\ln f_{\text{sh}})/\partial(\ln p)$. The green solid lines display the

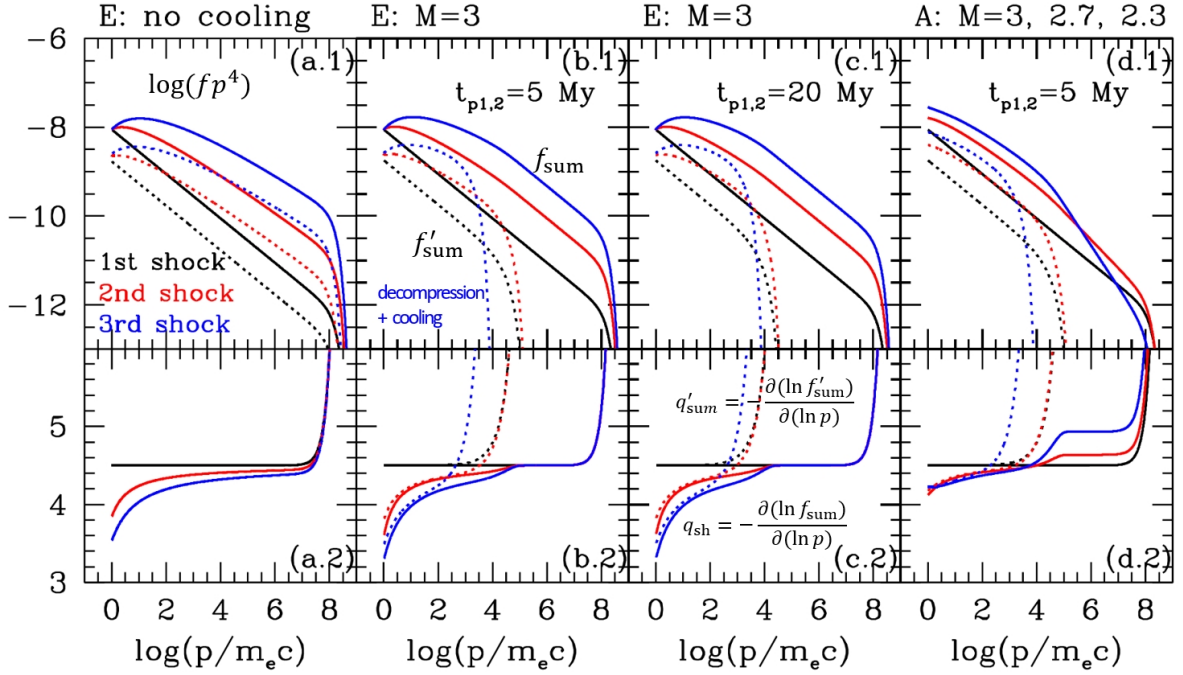


Figure 3. (a.1)-(d.1) Spectrum of CR electrons accelerated by three shocks: from left to right, mode E without cooling, with $t_{p1,2} = 5$ Myr, $t_{p1,2} = 20$ Myr, and model A with $t_{p1,2} = 5$ Myr. Here $t_{p1,2} = t_{p1} = t_{p2}$ is the time interval between two consecutive shocks. The third shock lasts for $t_{p3} = 100$ Myr. The solid lines show $f_{sh}(p) = f_{sum}(p)$ at the shock, while the dotted lines show $f'_{sum}(p)$ at the far-downstream region. (a.2)-(d.2) Power-law slopes, $q_{sh} = -\partial(\ln f_{sum})/\partial(\ln p)$ at the shock (solid lines) and $q'_{sum} = -\partial(\ln f'_{sum})/\partial(\ln p)$ at the far-downstream region (dotted lines). The injection parameter, the density reduction factor, and the preshock magnetic field strength are set to be $Q_e = 3.8$, $\mathcal{D} = 1$, and $B_1 = 1 \mu\text{G}$. For the IC cooling term, the redshift is set as $z = 0.2$. The black, red, and blue lines are used for $k = 1, 2, \text{ and } 3$, respectively.

DSA slope for the third shock, $q_3 = 3r_3/(r_3 - 1)$ (green solid), while the green dot-dashed lines display $q_3 + 1$ (green dot-dashed).

In the next subsection we focus on the radio synchrotron spectrum in the frequency range of $\nu_1 \lesssim \nu \lesssim \nu_2$, whose emission comes mainly from electrons in the energy range of $\gamma_1 \lesssim \gamma_e \lesssim \gamma_2$ (see Equations (12)):

$$\gamma_{1,2} \approx 5.1 \times 10^3 \left(\frac{\nu_{1,2}}{0.1 \text{ GHz}} \right)^{1/2} \left(\frac{\langle B_2 \rangle}{3 \mu\text{G}} \right)^{-1/2}, \quad (14)$$

where $\nu_1 = 0.1$ GHz, $\nu_2 = 10$ GHz, and $\langle B_2 \rangle$ is the mean postshock magnetic field strength. In the upper two rows of Figure 4, the vertical black dotted lines indicate γ_1 and γ_2 for the third shock with M_3 and $B_1 = 1 \mu\text{G}$.

Comparing $f_{sh}(p)$ of radio emitting electrons among the three models shown in Figure 4, we find the following. (1) Model A with $t_{p1,2} = 5$ Myr suffers less cooling, and so retains more substantial effects of multiple shocks in the range of $\gamma_1 \lesssim \gamma_e \lesssim \gamma_2$, compared to the model with $t_{p1,2} = 20$ Myr. (2) Model B with $M_3 = 3$ has a flatter spectrum than model A with $M_3 = 2.3$, but $q_{sh,3}$ exhibits very little multiple shock effects in the same range of γ_e (see the magenta line in panel (c.2)).

The amplitude of $F(p)$ at the first and second shocks, especially at low energies, is larger in the model with $t_{p1,2} = 20$ Myr than that with $t_{p1,2} = 5$ Myr,

because the postshock advection length increases with time as $d = u_2 t_{p1,2}$. For both the models, however, $t_{p3} = 100$ Myr is the same, so the amplitude of $F(p)$ at the third shock (blue solid lines) is similar. As expected, $F(p)$ steepens gradually by one power of p above the break momentum at $\gamma_{e,br} \sim 10^4$ behind the third shock. So $q_{int,3}$ (blue solid) approach to $q_3 + 1$, while $q_{sh,3}$ (magenta dashed) approaches to q_3 at high energies. On the other hand, both the slopes are smaller (flatter) than the expected DSA slopes for $\gamma_e \lesssim 10^3 - 10^5$ due to the re-acceleration by multiple shocks. In particular, the effects of multiple shocks could persist for radio-emitting electrons with $\gamma_1 \lesssim \gamma_e \lesssim \gamma_2$ (between the two vertical black dotted lines), if $t_{p1,2} \lesssim 20$ Myr and the Mach numbers of the preceding shocks are higher than that of the last shock (i.e., model A).

The left panels of Figure 5 compare $F(p)$ for the four cases with different $B_1 = 0.01, 0.1, 1, \text{ and } 2 \mu\text{G}$ for model A. Panels (a.1)-(a.2) show that $F(p)$ depends rather weakly on B_1 , because the effective field strength, $B_e \sim 5 \mu\text{G}$, varies a little for the range of B_1 considered here.

The middle and right panels of Figure 5 show models C and D with $t_{p1,2} = 5$ Myr and $B_1 = 1 \mu\text{G}$ (see Table 1). Again they demonstrate that the effects of multiple shocks are important only for the case in which the preceding shocks are stronger than the last shock (model C). In other words, the CR electrons, accelerated by weaker preceding shocks and then cooled in the post-

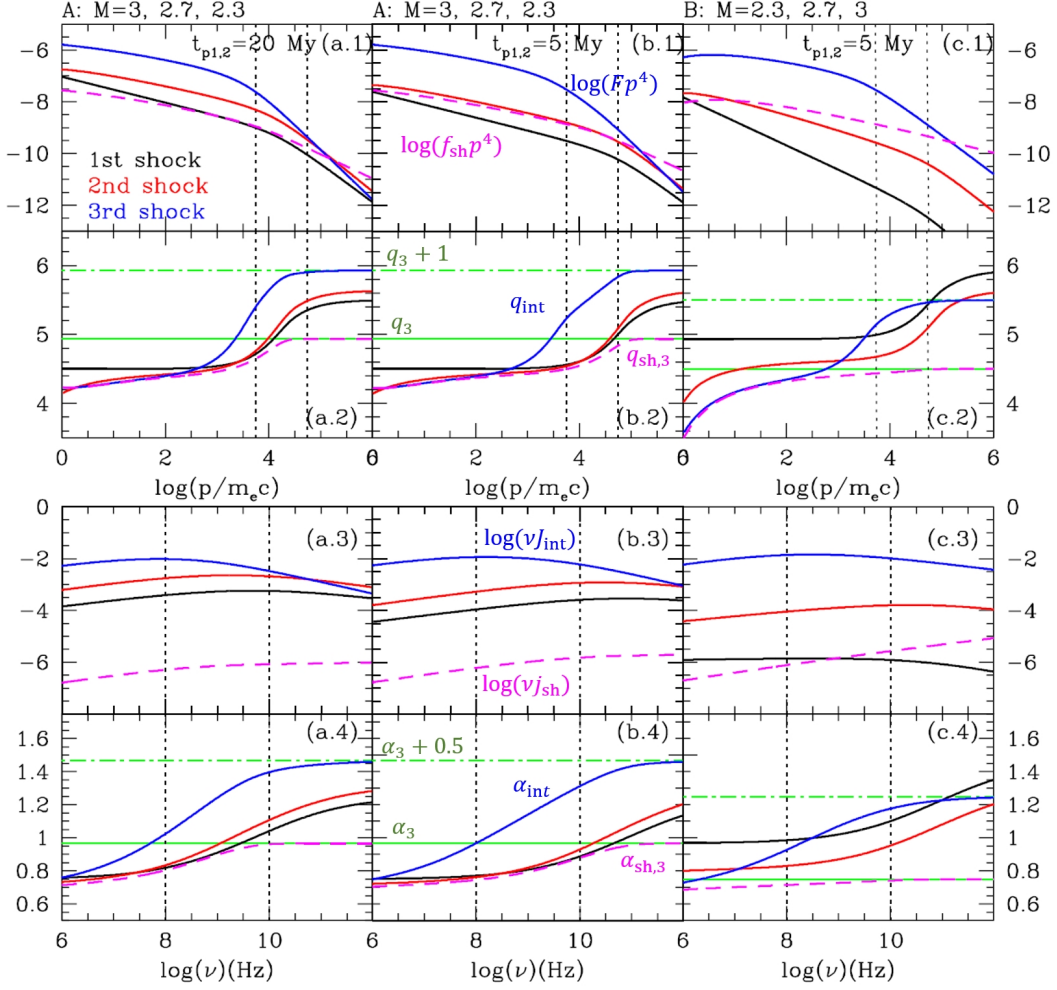


Figure 4. DSA by three different shocks: model A with $M = 3, 2.7,$ and 2.3 with $t_{p1,2} = 20$ Myr (left column) and 5 Myr (middle column) and model B with $M = 2.3, 2.7,$ and 3 with $t_{p1,2} = 5$ Myr (right column). (a.1)-(c.1) Volume-integrated spectrum, $F(p)$, at each shock (black, red, and blue solid lines) and postshock spectrum, $f_{sh}(p)$, at the third shock (magenta dashed lines). The vertical black dotted lines indicate γ_1 and γ_2 in Equation (14) for the third shock defined with M_3 and $B_1 = 1 \mu\text{G}$. (a.2)-(c.2) Power-law slopes, $q_{int} = -\partial(\ln F)/\partial(\ln p)$ and $q_{sh,3} = -\partial(\ln f_{sh})/\partial(\ln p)$. The green dotted lines show the DSA power-law slope, $q_3 = 3r_3/(r_3 - 1)$ at the third shock, while the green dot-dashed lines show, $q_3 + 1$. (a.3)-(c.3) Volume-integrated radio spectrum, $J_{int}(\nu)$, at each shock (black, red, and blue solid lines) and postshock radio spectrum, $j_{sh}(\nu)$, at the third shock (magenta dashed lines). The vertical black dotted lines show $\nu_1 = 0.1$ GHz and $\nu_2 = 10$ GHz. (a.4)-(c.4) Radio spectral index, $\alpha_{int} = -\partial(\ln J_{int})/\partial(\ln \nu)$ and $\alpha_{sh,3} = -\partial(\ln j_{sh})/\partial(\ln \nu)$.

shock region, provide only low-energy seed electrons. So they could increase somewhat the amplitude of f_{sh} , but do not affect substantially the power-law slope (model D).

3.3. Integrated Radio Spectrum

The lower two rows of Figures 4 and 5 compare the radio synchrotron emission spectra for the respective models shown in the upper two rows. Panels (a.3)-(c.3) show the volume-integrated radio spectrum, $\nu J_{int}(\nu)$, at each shock and the postshock spectrum, $\nu j_{sh}(\nu)$, at the third shock, while panels (a.4)-(c.4) show $\alpha_{int} = -d \ln J_{int} / d \ln \nu$ (solid lines) and $\alpha_{sh} = -d \ln j_{sh} / d \ln \nu$ (magenta dashed lines). The green solid lines display the DSA slope for the third shock, $\alpha_3 = (q_3 - 3)/2$, while the green dot-dashed lines display $\alpha_3 + 0.5$. Exceptions are panels (a.3) and (a.4) of Figure 5, where

only J_{int} and α_{int} are shown for model A with different values of B_1 .

As noted above, the slope of $J_{int}(\nu)$ increases gradually from α_{sh} to $\alpha_3 + 0.5$ over a very broad range of the frequency (i.e., so-called CI case), where the break frequency, $\nu_{br} \sim 0.3$ GHz. At high frequencies, $\alpha_{int,3}$ (blue solid) approaches to $\alpha_3 + 0.5$, while $\alpha_{sh,3}$ (magenta dashed) approaches to α_3 . On the other hand, panel (b.4) of Figure 4 shows that $\alpha_{sh,3} < \alpha_3$ and $\alpha_{int,3} < \alpha_3 + 0.5$ for $\nu \lesssim 10$ GHz, reflecting the flattening effects of multiple shocks in model A. In model C, panel (b.4) of Figure 5 exhibit the same behaviors for even higher frequencies.

Unlike $F(p)$, $J_{int}(\nu)$ depends sensitively on B_1 , as can be seen in panels (a.3)-(a.4) of Figure 5. This is because cooling is dominated by iC scattering off back-

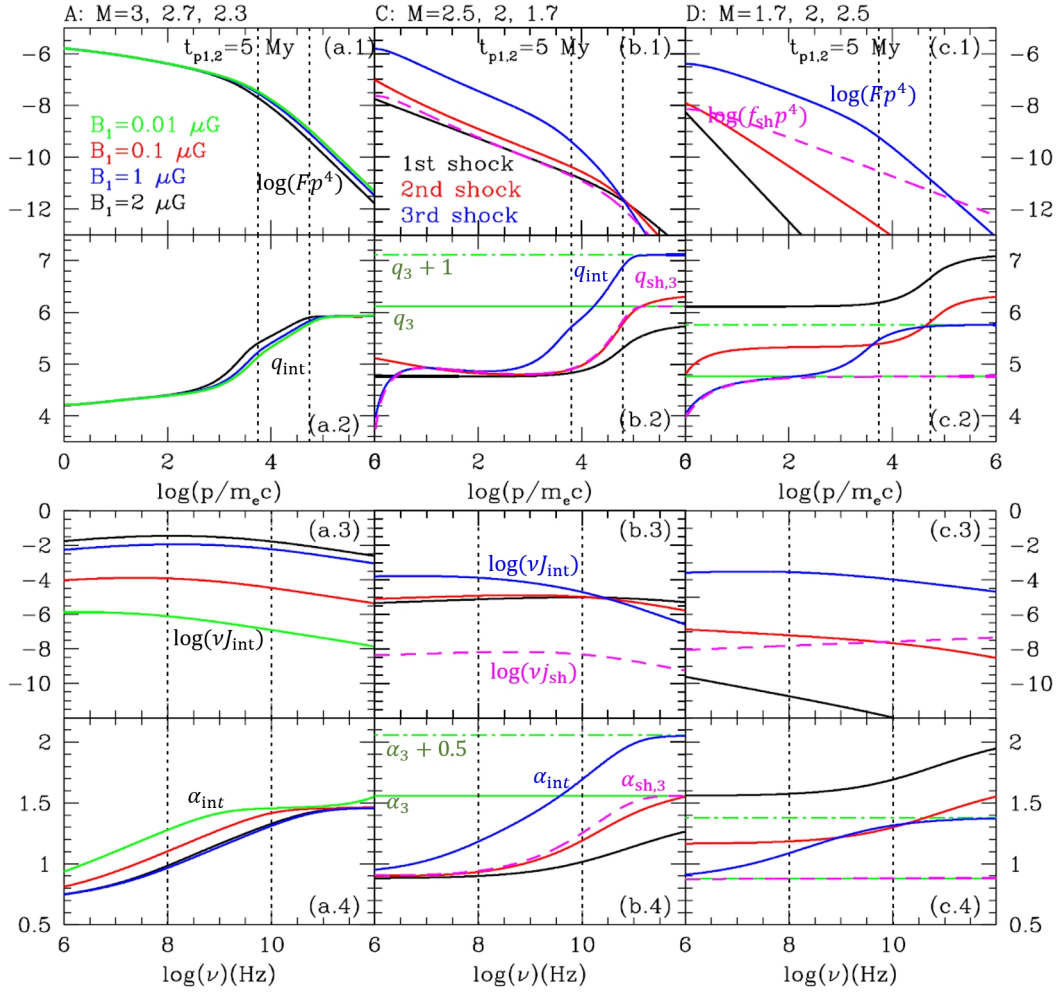


Figure 5. Same as Figure 4 except the A model with different B_1 (left column), and models C (middle column) and D (right column) with $B_1 = 1 \mu\text{G}$ are presented. The shock passage time, $t_{p1,2} = 5 \text{ Myr}$, is adopted. See Table 1 for the model parameters.

ground photons for the range of B_1 considered here, while the radio synchrotron spectrum scales roughly with B_1 . For model A with $B_1 = 0.01 \mu\text{G}$ (green solid), $J_{\text{int}}(\nu)$ is almost a single power-law and $\alpha_{\text{int},3} \approx \alpha_3 + 0.5$ for $\nu > 1 \text{ GHz}$.

In short, the flattening of the radio spectrum at the shock, $j_{\text{sh}}(\nu)$, or the volume-integrated radio spectrum, $J_{\text{int}}(\nu)$, due to multiple re-acceleration is significant, only if the preceding shocks are stronger than the last shock as in models A and C. The volume-integrated spectrum $J_{\text{int}}(\nu)$ steepens gradually over a very broad frequency range.

3.4. Radio Spectral Index

If a radio relic is generated by three shock passages as in model A, $J_{\text{int}}(\nu)$ would not be a single power-law, but exhibit a spectral curvature at high frequencies, as shown in Figure 4. Then, inferring the Mach number of the radio relic shock from the relation $M_{\text{rad}} = [(\alpha_{\text{int}} + 1)/(\alpha_{\text{int}} - 1)]^{1/2}$ may result in incorrect results, when the slope α_{int} is estimated between two observation frequencies, for instance, $0.1 \text{ GHz} \lesssim \nu_{\text{obs},1}, \nu_{\text{obs},2} \lesssim 10 \text{ GHz}$.

To examine this problem, we plot the spectral index $\alpha_{0.61}$ of $j_{\text{sh},3}(\nu)$ at 0.61 GHz versus the predicted DSA index, $\alpha_3 = 0.5(M_3^2 + 3)/(M_3^2 - 1)$, of the third shock in the left panel of Figure 6. The spectral index $\alpha_{0.15}^{1.5}$ of the volume-integrated spectrum, J_{int} , between 0.15 and 1.5 GHz is shown against $\alpha_3 + 0.5 = (M_3^2 + 1)/(M_3^2 - 1)$ of the third shock in the right panel of Figure 6. In models A and C, $\alpha_{0.61}$ is smaller than α_3 due to the multiple re-acceleration effects, and the difference between the two indices is greater for smaller $t_{p1,2}$. In the case of $t_{p1,2} = 100 \text{ Myr}$ (asterisks), $\alpha_{0.61} \approx \alpha_3$, because the multiple shock effects disappear due to postshock cooling. On the other hand, $\alpha_{0.61} \approx \alpha_3$ in models B and D, regardless of $t_{p1,2}$, so the three symbols almost overlap each other.

By contrast, α_{int} is smaller than $\alpha_3 + 0.5$ for all the cases shown except model A with $B_1 = 0.01 \mu\text{G}$ (magenta triangle). This is because J_{int} steepens and exhibits spectral curvature over a very broad range of frequencies. The difference between the two indices is the greatest in model C (red symbols). For model A with $B_1 = 0.01 \mu\text{G}$, the break frequency is low enough,

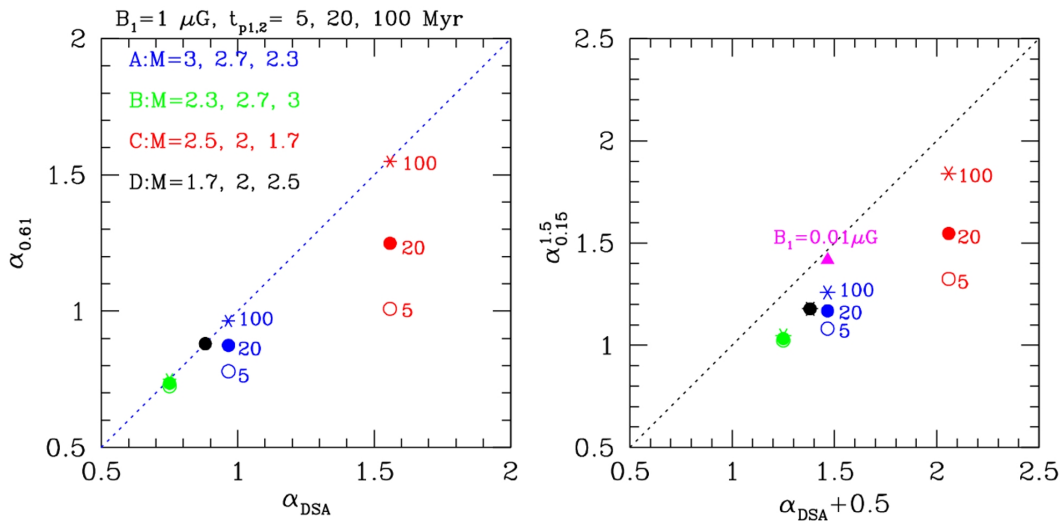


Figure 6. Left: Radio spectral index $\alpha_{0.61}$ of the shock spectrum $j_{\text{sh},3}(\nu)$ at 0.61 GHz versus the predicted DSA index, $\alpha_{\text{DSA}} = 0.5(M_3^2 + 3)/(M_3^2 - 1)$, of the third shock. Right: Radio spectral index $\alpha_{0.15}^{1.5}$ of the volume-integrated spectrum J_{int} between 0.15 and 1.5 GHz versus the predicted DSA index, $\alpha_{\text{DSA}} + 0.5 = (M_3^2 + 1)/(M_3^2 - 1)$ of the third shock. The results for the A (blue), B (green), C (red), and D (black) models with $t_{\text{p}1,2} = 5$ Myr (open circles), 20 Myr (filled circles), and 100 Myr (asterisks) and $B_1 = 1 \mu\text{G}$ are shown, except for the magenta triangle (model A with $t_{\text{p}1,2} = 5$ Myr and $B_1 = 0.01 \mu\text{G}$). For the B and D models, the three different symbols almost overlap each other.

$\nu_{\text{br}} \sim 1$ MHz, so J_{int} becomes almost a single power-law between 150 MHz and 1.5 GHz.

This exercise illustrates that the estimation of the shock Mach number from radio spectral indices, α_{sh} or α_{int} , at certain observation frequencies should be made with cautions, since the emission spectrum could be affected by any preceding shocks. In model A with $M_3 = 2.3$ and $t_{\text{p}1,2} = 5$ Myr, for instance, the Mach number estimated from $\alpha_{0.61} \approx 0.78$ would be $M_{\text{rad}} \approx 2.9$, while that estimated from $\alpha_{0.15}^{1.5} \approx 1.08$ would be $M_{\text{rad}} \approx 5.0$. Hence, both the estimates would be higher than the X-ray inferred value, $M_X \approx M_3$.

In observations of real radio relics, however, J_{int} depends on the three-dimensional shape of the postshock region and the viewing angle relative to the shock surface. Modeling of more realistic configuration is beyond the scope of this study.

4. SUMMARY

We have examined the re-acceleration of CR electrons by multiple shocks that formed in the turbulent ICM during mergers of galaxy clusters. We assume that the momentum distribution function of the accelerated electrons, $f_{\text{sh}}(p)$, develops a suprathermal power-law tail for $p \geq p_{\text{ref}} \sim 3.8p_{\text{the}}$, which extends beyond the injection momentum p_{inj} for full DSA (see Equation (5)). Moreover, suprathermal electrons are presumed to be re-accelerated via DSA for $p \geq p_{\text{ref}}$ as well (see Equation (8)). Following the work of Kang (2021), the accelerated CRs are assumed to undergo adiabatic decompression by a factor of $R = r^{-1/3}$ behind each shock (see Melrose & Pope 1993). A simple decompression model for the postshock magnetic field, $B_2(x)$, is also adopted to estimate synchrotron energy losses and emission spectrum in the postshock region.

We have considered the several examples with three shocks with the sonic Mach numbers, $M = 1.7 - 3$, whose parameters are listed in Table 1. The main findings can be summarized as follows:

1. The effects of multiple shocks are significant only for the cases, in which the preceding shocks are stronger than or equal to the last shock, i.e. $M_1, M_2 \geq M_3$ (e.g., A, C, and E models). Moreover, the passage times between consecutive shocks should be $t_{\text{p}1,2} \lesssim 20$ Myr in order to retain a substantial amount of high-energy electrons after cooling in the postshock region.
2. For radio emitting electrons with $\gamma_e \approx 10^4 - 10^5$, the amplitude of $f_{\text{sh}}(p)$ increases by a factor of about 5 – 10 at each passage of a $M \sim 3$ shock (see Figure 3). For weaker shocks, the amplification factor due to re-acceleration is lower.
3. As in the case of CR protons (Kang 2021), multiple shock passages flatten the the CR spectrum from low energies and upward. So the slope of $f_{\text{sh}}(p)$ at the third shock is smaller (flatter) than the DSA slope, i.e., $q_{\text{sh},3} < q_3 = 3r_3/(r_3 - 1)$, for low-energy electrons with $\gamma_e \lesssim 10^4$.
4. The flattening of $f_{\text{sh}}(p)$ and $F(p)$ leads to the flattening of radio spectrum, $j_{\text{sh}}(\nu)$, and the volume-integrated spectrum, $J_{\text{int}}(\nu)$ at the third shock (see Figures 4 and 5).
5. The slope of $J_{\text{int}}(\nu)$ steepens gradually from α_{sh} to $\alpha_3 + 0.5$ over a very broad frequency range. As a result, both α_{sh} and α_{int} tend to be smaller than the DSA-predicted slopes of $\alpha_3 = (q_3 - 3)/2$ and $\alpha_3 + 0.5$, respectively (see Figure 6). This implies that the estimation of the shock Mach number from

observed spectral indices, α_{sh} or α_{int} , should be made with caution.

6. In the opposite cases with $M_1, M_2 < M_3$ (e.g. B and D models), the electrons accelerated by the preceding shocks provide only low-energy seed electrons to DSA without significant flattening of $f_{\text{sh}}(p)$.
7. In the case of weak magnetic fields of $B_1 \lesssim 0.01 \mu\text{G}$, the volume-integrated radio spectrum, $j_{\text{int}}(\nu)$ becomes approximately a single power-law for $\nu \approx 0.1 - 10 \text{ GHz}$, because the break frequency becomes $\nu_{\text{br}} \sim 0.01 \text{ GHz}$.

We suggest that the re-acceleration by multiple shocks may explain the high DSA efficiency of CR electrons at weak ICM shocks and the discrepancies, $M_x \lesssim M_{\text{rad}}$, found in some radio relics (Akamatsu & Kawahara 2013; Hong et al. 2015; van Weeren et al. 2019; Inchingolo et al. 2021). For instance, in the case of $M_1, M_2 > M_3$, the X-ray Mach number is determined by the third shock, i.e., $M_x \approx M_3$, while the radio Mach number inferred from α_{sh} and α_{int} are affected the accumulated effects of all three shocks, and so it could be $M_{\text{rad}} > M_3$.

ACKNOWLEDGMENTS

This work was supported by the National Research Foundation (NRF) of Korea through grants 2016R1A5A1013277 and 2020R1F1A1048189.

REFERENCES

- Akamatsu, H., & Kawahara, H. 2013, Systematic X-Ray Analysis of Radio Relic Clusters with Suzaku, *PASJ*, 65, 16
- Achterberg, A. 1990, Particle Acceleration by an Ensemble of Shocks, *A&A*, 231, 251
- Brunetti, G., & Jones, T. W. 2014, Cosmic Rays in Galaxy Clusters and Their Nonthermal Emission, *Int. J. of Modern Physics D*, 23, 30007
- Caprioli, D., Pop, A. R., & Spitkovsky, A. 2015, Simulations and Theory of Ion Injection at Non-relativistic Collisionless Shocks, *ApJ*, 798, 28
- Carilli, C. L., Perley, R. A., Dreher, J. W., & Leahy, J. P. 1991, Multifrequency Radio Observations of Cygnus A: Spectral Aging in Powerful Radio Galaxies, *ApJ*, 383, 554
- Di Gennaro, G., van Weeren, R. J., Hoef, M. et al. 2018, Deep Very Large Array Observations of the Merging Cluster CIZA J2242.8+5301: Continuum and Spectral Imaging *ApJ*, 865, 24
- Domínguez-Fernández, P., Brügggen, M., Vazza, F. et al. 2021, Morphology of Radio Relics – I. What Causes the Substructure of Synchrotron Emission?, *MNRAS*, 500, 795
- Drury, L. O’C. 1983, An Introduction to the Theory of Diffusive Shock Acceleration of Energetic Particles in Tenuous Plasmas, *Rep. Prog. Phys.*, 46, 973
- Gieseler, U. D. J. & Jones, T. W. 2002, First order Fermi acceleration at multiple oblique shocks, *A&A*, 357, 1133
- Guo, F., & Giacalone, J. 2015, The Acceleration of Electrons at Collisionless Shocks Moving Through a Turbulent Magnetic Field, *ApJ*, 802, 97
- Guo, X., Sironi, L., & Narayan, R. 2014, Non-thermal Electron Acceleration in Low Mach Number Collisionless Shocks. I. Particle Energy Spectra and Acceleration Mechanism, *ApJ*, 793, 153
- Ha, J.-H., Ryu, D., & Kang, H. 2018a, Properties of Merger Shocks in Merging Galaxy Clusters, *ApJ*, 857, 26
- Ha, J.-H., Ryu, D., Kang, H., & van Marle, A. J. 2018b, Proton Acceleration in Weak Quasi-parallel Intracluster Shocks: Injection and Early Acceleration, *ApJ*, 864, 105
- Ha, J.-H., Kim, S., Ryu, D., & Kang, H. 2021, Effects of Multi-scale Plasma Waves on Electron Preacceleration at Weak Quasi-perpendicular Intracluster Shocks, *arXiv e-prints*, arXiv:2102.03042.
- Hong, S., Kang, H., & Ryu, D. 2015, Radio and X-ray Shocks in Clusters of Galaxies, *ApJ*, 812, 49
- Inchingolo, G., Wittor, D., Rajpurohit, K., Vazza, F. 2021, Radio relics radio emission from multi-shock scenario, *MNRAS*, 000, 00
- Jaffe, W. J., & Perola, G. C. 1973, Dynamical Models of Tailed Radio Sources in Clusters of Galaxies, *A&A*, 26, 423
- Kang, H. 2011, Energy Spectrum of Nonthermal Electrons Accelerated at a Plane Shock, *JKAS*, 44, 49
- Kang, H. 2015, Nonthermal Radiation from Relativistic Electrons Accelerated at Spherically Expanding Shocks *JKAS*, 48, 9
- Kang, H. 2016, Reacceleration Model for the ‘Toothbrush’ Radio Relic, *JKAS*, 49, 83
- Kang, H. 2020, Semi-analytic Models for Electron Acceleration in Weak ICM Shocks, *JKAS*, 53, 59
- Kang, H. 2021, Diffusive Shock Acceleration by Multiple Weak Shocks, *JKAS*, 54, 103 (Paper I)
- Kang, H., Jones, T. W., & Gieseler, U. D. J. 2002, Numerical Studies of Cosmic-Ray Injection and Acceleration, *ApJ*, 579, 337
- Kang, H., & Ryu, D. 2010, Diffusive Shock Acceleration in Test-particle Regime, *ApJ*, 721, 886
- Kang, H., Ryu, D., & Jones, T. W. 2012, Diffusive Shock Acceleration Simulations of Radio Relics, *ApJ*, 756, 97
- Kang, H., Ryu, D., & Jones, T. W. 2017, Shock Acceleration Model for the Toothbrush Radio Relic, *ApJ*, 840, 42
- Kang, H., Ryu, D., & Ha, J.-H. 2019, Electron Preacceleration in Weak Quasi-perpendicular Shocks in High-beta Intracluster Medium, *ApJ*, 876, 79
- Kobzar, O., Niemiec, J., Amano, T., et al. 2021, Electron Acceleration at Rippled Low-Mach-number Shocks in High-beta Collisionless Cosmic Plasmas, *arXiv:2107.00508*
- Melrose D.B., & Pope M.H., 1993, Diffusive Shock Acceleration by Multiple Shocks, *Proc. Astron. Soc. Aust.* 10, 222
- Park, J., Caprioli, D., & Spitkovsky, A. 2015, Simultaneous Acceleration of Protons and Electrons at Nonrelativistic Quasiparallel Collisionless Shocks, *PRL*, 114, 085003
- Rajpurohit, K., Hoeft, M., Vazza, F. et al., 2020, New Mysteries and Challenges from the Toothbrush Relic: Wide-band Observations from 550MHz to 8GHz, *A&A*, 636, A30
- Roh, S., Ryu, D., Kang, H., Ha, S., & Jang, H. 2019, Turbulence Dynamo in the Stratified Medium of Galaxy Clusters, *ApJ*, 883, 138
- Ryu, D., Kang, H., Hallman, E., & Jones, T. W. 2003, Cosmological Shock Waves and Their Role in the Large-Scale Structure of the Universe, *ApJ*, 593, 599

- Ryu, D., Kang, H., & Ha, J.-H. 2019, A Diffusive Shock Acceleration Model for Protons in Weak Quasi-parallel Intracluster Shocks, *ApJ*, 883, 60
- Schneider, P. 1993, Diffusive particle acceleration by an ensemble of shock waves, *A&A*, 278, 315
- Trotta, D., & Burgess, D. 2019, Electron Acceleration at Quasi-perpendicular Shocks in Sub- and Supercritical Regimes: 2D and 3D Simulations, *MNRAS*, 482, 1154
- van Weeren, R., Röttgering, H. J. A., Brüggén, M., & Hoeft, M. 2010, Particle Acceleration on Megaparsec Scales in a Merging Galaxy Cluster, *Science*, 330, 347
- van Weeren, R. J., Brunetti, G., Brüggén, M., et al. 2016, LOFAR, VLA, and CHANDRA Observations of the Toothbrush Galaxy Cluster, *ApJ*, 818, 204
- van Weeren, R. J., de Gasperin, F., Akamatsu, H., et al. 2019, Diffuse Radio Emission from Galaxy Clusters, *Space Science Reviews*, 215, 16
- Vazza, F., Brunetti, G., & Gheller, C. 2009, Shock Waves in Eulerian Cosmological Simulations: Main Properties and Acceleration of Cosmic Rays, *MNRAS*, 395, 1333
- Vazza, F., Dolag, K., Ryu, D., et al. 2011, A comparison of cosmological codes: properties of thermal gas and shock waves in large-scale structures, *MNRAS*, 418, 960
- White, R. L. 1985 Synchrotron Emission from Chaotic Stellar Winds, *ApJ*, 289, 698